

# The energy injection and losses in the Monte Carlo simulations of a diffusive shock

Xin, Wang,<sup>1,2</sup> Yihua, Yan<sup>1</sup>

**Abstract.** Although diffusive shock acceleration (DSA) could be simulated by some well-established models, the assumption of the injection rate from the thermal particles to the superthermal population is still a contentious problem. But in the self-consistent Monte Carlo simulations, because of the prescribed scattering law instead of the assumption of the injected function, hence particle injection rate is intrinsically defined by the prescribed scattering law. We expect to examine the correlation of the energy injection with the prescribed multiple scattering angular distributions. According to the Rankine-Hugoniot conditions, the energy injection and the losses in the simulation system can directly decide the shock energy spectrum slope. By the simulations performed with multiple scattering law in the dynamical Monte Carlo model, the energy injection and energy loss functions are obtained. As results, the case applying anisotropic scattering law produce a small energy injection and large energy losses leading to a soft shock energy spectrum, the case applying isotropic scattering law produce a large energy injection and small energy losses leading to a hard shock energy spectrum.

## 1. Introduction

The gradual solar energetic particles with a power-law energy spectrum are generally thought to be accelerated by the first-Fermi acceleration mechanism at the interplanetary shocks (IPs) [Azford *et al.*, 1977; Krymsky, 1977; Bell, 1978; Blandford and Ostriker, 1978]. It is well known that the diffusive shock accelerated the particles efficiently by the accelerated particles scattering off the instability of Alfvén waves which are generated by the accelerated particles themselves [Lagage and Cesarsky, 1983; Gosling *et al.*, 1981; Cane *et al.*, 1990; Lee and Ryan, 1986; Pelletier *et al.*, 2006; Li *et al.*, 2009]. The diffusive shock acceleration (DSA) is so efficient that the back-reaction of the accelerated particles on the shock dynamics cannot be neglected. So the theoretical challenge is how to efficiently model the full shock dynamics [Caprioli *et al.*, 2010; Zank, 2000; Li *et al.*, 2003; Lee, 2005]. To efficiently model the shock dynamics and the particles' acceleration, there are largely three basic approaches: stationary Monte Carlo simulations, fully numerical simulations, and semi-analytic solutions. In the stationary Monte Carlo simulations, the particle population with a prescribed scattering law is calculated based on the particle-in-cell (PIC) techniques [Ellison *et al.*, 1996; Vladimirov *et al.*, 2006]. In the fully numerical simulations, a time-dependent diffusion-convection equation for the CR transport is solved with coupled gas dynamics conservation laws [Kang and Jones, 2007; Zirakashvili and Aharonian, 2010]. In the semi-analytic approach, the stationary or quasi-stationary diffusion-convection equations coupled to the gas dynamical equations are solved [Blasi *et al.*, 2007; Malkov *et al.*, 2000]. Since the velocity distribution of superthermal particles in the Maxwellian tail is not isotropic in the shock frame, the diffusion-convection equation can-

not directly follow the injection from the non-diffusive thermal pool into the diffusive CR population. So considering both the quasi-stationary analytic models and the time-dependent numerical models, the injection of particles into the acceleration mechanism is based on an assumption of the transparency function for thermal leakage [Blasi *et al.*, 2005; Kang and Jones, 2007; Vainio and Laitinen, 2007] *a priori*. Thus, the dynamical Monte Carlo simulations based on the PIC techniques are expected to model the shock dynamics time-dependently and also can eliminate the suspicion arising from the assumption of the injection [Knerr *et al.*, 1996; Wang and Yan, 2011]. In plasma simulation (Monte Carlo model and hybrid model), since the proton's mass is very larger than the electron's mass, the total plasma can be treated as one species of proton fluid with a massless electronic fluid which just balance the electric charge state for maintaining a neutral fluid [Leroy *et al.*, 1982]. There is no distinction between thermal and non-thermal particles, hence particle injection is intrinsically defined by the prescribed scattering properties, and so it is not controlled with a free parameter [Caprioli *et al.*, 2010].

Actually, Wang and Yan [2011] have extended the dynamical Monte Carlo models invoking multiple scattering angular distributions. Unlike the previous KJE [Knerr *et al.*, 1996] dynamical Monte Carlo models invoking a purely isotropic scattering angular distribution, this multiple scattering law allow the particles are scattered by angles distributed with Gaussian functions. According to the simulations using the extended multiple scattering angular distributions, a series of similar energy spectrums with a little difference with respect of the power-law tail are obtained. And the results show that the energy spectral index is effected by the prescribed scattering law. Specifically, the total shock's energy spectral index is less than one and shows an increasing function of the dispersion of the scattering angular distribution, but the subshock's energy spectral index is more than one and shows a decreasing function of the dispersion of the scattering angular distribution.

In an effort to research why the multiple scattering angular distributions can produce the difference of the energy spectral index, it is necessary to analyze the energy injection and the energy losses in the entire simulation system. Because the energy injection and losses are important factors for deciding the acceleration efficiency and the energy

<sup>1</sup>Key Laboratory of Solar Activities of National Astronomical Observatories, Chinese Academy of Sciences, Beijing 100012, China

<sup>2</sup>State Key Laboratory of Space Weather, Chinese Academy of Sciences, Beijing 100080, China

spectrum slope owing to the Rankine-Hugoniot relationship based on the energy conservational law.

However, in the Monte Carlo simulation, the particle injection and the energy loss processes are treated in natural, self-consistent manner and decided by the prescribed scattering law. In order to obtain the complete energy injection and loss real-time functions in the entire simulation system, we perform the simulations by the multiple scattering law considering an improved simulation system. In this new simulation system, a radial reflective boundary (RRB) is set for preventing the energy losses via the radial diffusion. Under these scenarios, the performed simulation cases consist of four specific standard deviation values of the Gaussian distribution function.

In Section 2, the basic simulation method is introduced with respect to the Gaussian scattering angular distributions for obtaining the energy injection and loss functions of time in each case. In Section 3, we present the energy analysis for all cases with four types of scattering angle distributions. Section 4 includes a summary and the conclusions.

## 2. Method

The Monte Carlo model is a general model, although it is considerably expensive computationally, and it is important in many applications to include the dynamical effects of non-linear DSA in simulations. Since the prescribed scattering law can replace the electromagnetic field calculation which is used in hybrid simulations [Giacalone, 2004; Winske and Omid, 2011], we assume that the individual particle scatters elastically off the background scattering centers with the scattering angles according to a Gaussian distribution in the local frame. And the particle's mean free path is proportional to the local velocities in its local frame with

$$\lambda = V_L \cdot \tau. \quad (1)$$

Where,  $\tau$  is the average scattering time. Under the prescribed scattering law, the injection is purely correlated with those particles from the “thermal pool” in the downstream region become into the superthermal particles [Ellison et al., 2005].

In these simulations, the entire shock is simulated in one-dimensional box as shown in Figure 1, the initial continually inflow enter into the box from the left boundary with a supersonic bulk velocity ( $U_0$ ), a stationary reflective wall at the right boundary of the box act to form a piston shock moving from right to left. After a certain time, a steady compression region (i.e. downstream region) will be formed in front of the reflective wall. The bulk velocity in downstream region is become to zero, since the particles dissipate in the downstream region and their large translational energy is converted into isotropic, random energy. To model the finite size of system and the lack of sufficient scattering far upstream to turn particles around [Mitchell et al., 1983], the presented simulation includes the escape of the energetic particles at an upstream “free escape boundary” (FEB). This FEB moves with the shock front at a shock velocity ( $V_{sh}$ ) and remains a constant distance in front of the shock position (i.e.  $X_{FEB}=90$ ). This distance is enough large for majority of the injected particles diffuse between the foreshock region and the downstream region. The size of the foreshock is the distance from the shock to the FEB and thus sets a limit on the maximum energy a particle can obtain. Since the injected particles cross the shock and diffuse upstream, they negatively contribute to the bulk velocity, and the bulk velocity become smaller and smaller from the FEB to the shock position. Holding the length of the foreshock region constant eventually (when enough time

has elapsed to create a larger number of accelerated particles) produces a steady state with respect to the amount of the energy entering and exiting the system from the upstream region. In addition, we set the radial boundary as  $R_{y,z} = 50$  for preventing particle's perpendicular diffusion to the infinity. Simultaneously, The radial reflective boundary can ensure the particles have efficient diffusive processes in the one-dimensional system along  $\hat{x}$  direction. So we are able to compare the difference of the energy injection and losses obtained from each case. We can further investigate the possibility that the cases applying anisotropic scattering angular distribution would produce a different acceleration efficiency compared with the case applying an isotropic scattering angular distributions. So an anisotropic scattering law in the theory of the CR-diffusion is also needed [Bell, 2004].

According to particle-in-cell (PIC) techniques [Forsslund, 1985; Spitkovsky, 2003; Nishikawa et al., 2008], the total box length in this simulation system is  $X_{max}=300$ , and it is divided up into  $n_x=600$  grids. The initial number of particles in each grid is  $n_0=650$ . In addition, we use a flux-weighted inflow to ensure the particles entering into the box with the same density flow in upstream with the time. This inflow in “preinflow box” (PIB) is put in the left boundary of the simulation box. The total simulation time  $T_{max} = 2400$ , and it is divided into the number of time steps  $N_t = 72000$  with a time step  $dt = 1/30$ . The size of the FEB distant from the shock front is set as  $X_{feb} = 90$ . The radii of the radial reflective boundary is set as  $R_{y,z} = 50$ . These simulation codes consist of the three substeps. (i) Individual particles move along the  $\hat{x}$ ,  $\hat{y}$ , and  $\hat{z}$  axis with their local velocities in each component, respectively.

$$x = x_0 + v_x \cdot t \quad y = y_0 + v_y \cdot t \quad z = z_0 + v_z \cdot t \quad (2)$$

Since the magnetic field  $B_0$  is parallel to the simulated shock's normal direction, the fluid quantities only vary in the  $\hat{x}$  direction. (ii) Collect the moments. Summation of particle masses and velocities are collected on a background computational grid based on PIC techniques. In this substep, the statistical average bulk speed of each grid represents the velocity of each scattering center. Once the value of the bulk speed drops to zero, the position of the shock front is decided by the displacement of the corresponding grid, and it means that the shock position is moved with an evolutionary velocity  $v_{sh}$  far away to the stationary reflected wall. Simultaneously, the size of the downstream region is extended dynamically with a constant velocity  $v_{sh}$ . Similarly, the foreshock region or precursor with a bulk velocity gradient is formed by the “back pressure” of the backward diffused particles. The moving of the FEB is also parallel to the shock moving with the same constant velocity  $v_{sh}$ . (iii) Applying multiple scattering laws. According to the scattering rate (i.e.  $R_s = dt/\tau$ , where  $R_s$  is the probability of the scattering events in time step  $dt$ , and  $\tau$  is the average scattering time). These fraction of the particles are chosen to scatter the background scattering centers with their corresponding scattering angles obeying to the given Gaussian distributions. The chosen particles scatter off the collected background with their local velocities and scattering angles. The scattered particles move along their path until they have new scatters. In the duration of the time step, if the all chosen particles have completed their scatters, the background bulk speed is subsequently changed. In the turn, the varied background bulk speed also will change the particle's individual velocity in the local frame in the next time step. The entire simulation time consists of the number of ( $N_t = 72000$ ) time step involving the above three substeps.

These presented simulations are all based on one-dimensional simulation box and the all simulated parameters has been described in detail elsewhere [Wang and Yan, 2011]. Here we list the simulation parameters in the Table

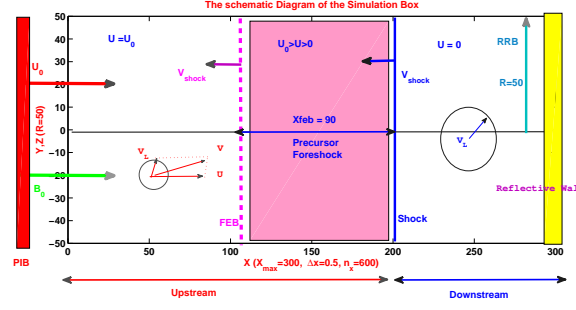


**Figure 1.** Schematic diagram of the simulation box. The shock is produced by incoming flow toward the reflective wall at the right boundary of the box ( $X_{\max}=300$ , Radial distance  $R=50$ ).

1. Upstream supersonic flow  $U_0$  with an initial Maxwellian thermal velocity  $V_L$  in their local frame and the inflow in a “pre-inflow box” (PIB) are both moving along one-dimensional simulation box from the left to the right. The parallel magnetic field  $B_0$  is along the  $\hat{x}$  axis direction. FEB with a constant length  $X_{feb} = 90$  in front of the shock position. The radial reflective boundary (RRB) is set as  $R_{y,z} = 50$ . The simulation box is dynamically consist of three regions: upstream, precursor and downstream. The bulk fluid speed in upstream region is  $U = U_0$ , the bulk fluid speed in downstream region is  $U = 0$ , and the bulk fluid speed with a gradient of velocity in the precursor region is  $U_0 > U > 0$ . To obtain the detailed information of the total particles in the simulation processes at any instant of time, we should build a large database for recording the velocities, positions, and the elapsed time of the all particles, as well as the indices and the bulk speeds of the total grids. Then we can obtain the energy spectrums from the downstream, precursor, and upstream regions. The escaped particles’ mass, momentum, and energy losses via the FEB can be also obtained. By analyzing the particle injection in the downstream region and the energy losses via FEB in the precursor region, we can find that how the prescribed scattering law to affect the shock compression ratio and the energy spectral index.

To examine the relationships between the shock energy spectral index and the prescribed scattering law by the energy injection and loss functions, we perform the Monte Carlo simulations with multiple scattering angular distributions using a new simulation system based on Matlab platform. The simulated cases are presented by Gaussian function with a standard deviation  $\sigma$  and an average value (i.e., the expect value)  $\mu = 0$  involving four cases: (1) Case A:  $\sigma = \pi/4$ . (2) Case B:  $\sigma = \pi/2$ . (3) Case C:  $\sigma = \pi$ . (4) Case D: isotropic distribution.

### 3. Energy analysis

#### 3.1. Shock structures

We present the entire shock evolution with the velocity profiles of the time sequences in each case as shown in Figure 2. The continuous inflow with a supersonic velocity  $U_0$  move from the left boundary ( $X = 0$ ) of the upstream region to the downstream region at the right of the box with the time. The total bulk speed profiles are consist of three regions with the time: the upstream region  $U = U_0$ , precursor region  $0 < U < U_0$ , and downstream region  $U = 0$ . Total profiles of the bulk speed is distinct by two positions of the FEB and the shock front with the time. From the Cases A, B, and C to D, the precursor explicitly shows an increasing slope of the bulk speed, the shock’s position  $X_{sh}$  also shows an increasing displacement increment in the  $\hat{X}$  axis at the end of the simulation, respectively. This means the shock evolves with an increasing velocity  $V_{sh}$  from the Cases A, B, and C to D, respectively. The simulated results of the dynamical shock in four cases are listed in the Table 2. In addition, by introducing a radial reflective boundary (RRB) in the present simulations, we also obtain the difference of the shock front position  $\Delta X_{sh}$  compared with the previous simulations [Wang and Yan, 2011] with an increasing value of the  $(\Delta X_{sh})_A = -3.5$ ,  $(\Delta X_{sh})_B = +6$ ,  $(\Delta X_{sh})_C = +6$ , and  $(\Delta X_{sh})_D = +17.5$  from the Cases A, B, and C to D, respectively. It is obvious to see that the affection of the RRB enhances this difference of the simulated shock for the four cases using the multiple scattering angular distributions.

According to the relationships between the upstream and the downstream, we are able to calculate the total shock compression ratio  $r_{tot}$  in the shock frame in each case as followings.

$$r_{tot} = \frac{U_0 + |V_{sh}|}{|V_{sh}|} \quad (3)$$

**Table 1.** The Simulation Parameters

Physical parameters	Dimensionless Value	Scaled Value
Inflow velocity	$u_0 = 0.3$	403km/s
Thermal speed	$v_0 = 0.02$	26.9km/s
Scattering time	$\tau = 0.833$	0.13s
Box size	$X_{max} = 300$	$10R_e$
Total time	$t_{max} = 2400$	6.3minutes
Time step size	$dt = 1/30$	0.0053s
Number of zones	$nx = 600$	...
Initial particles per cell	$n_0 = 650$	...
FEB distance	$X_{feb} = 90$	$3R_e$
Radial distance	$R_{y,z} = 50$	$\sim 1.5R_e$

Note: The Mach number  $M = 11.6$ . The  $R_e$  is the Earth’s radii. The data adapt from the Earth bow shock [Kner et al., 1996].

Different shock evolutionary velocity  $V_{sh}$  in different cases will probably lead to different dynamical shock structure. To showing this difference, we present the subtle velocity profiles at the end of simulation in each case in Figure 3. Evidently, the fluctuation of the velocity between the  $V_{sub}$  and  $V_d$  with an obviously increasing value from the Cases A, B, and C to D, respectively. And the specific structure in each plot consists of three main parts: precursor, subshock and downstream. The smooth precursor with a large scale is between the FEB and the subshock’s position  $X_{sub}$ , where the bulk velocity gradually drops from  $U_0$  to  $V_{sub}$ . The sharp subshock with a short scale just spans three-grid-length involving a deep drop of the bulk speed abruptly from  $v_{sub}$  to  $v_d$ , where the scale of the three-grid-length is about

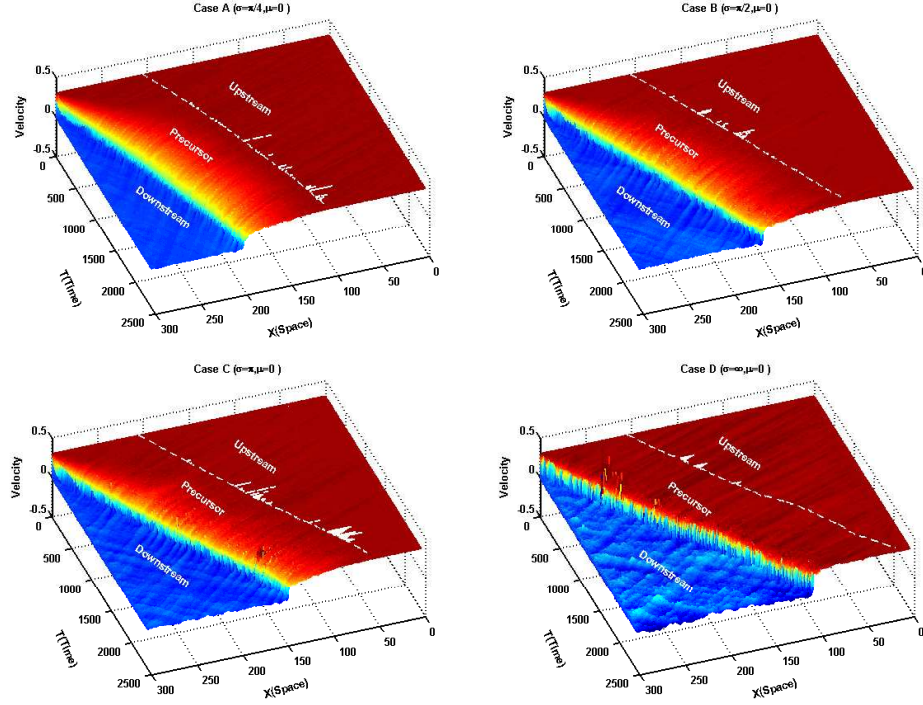


**Figure 2.** The entire evolutionary velocity profiles in four cases. The dashed line denotes the FEB position in each plot. The precursor is located in the area between the downstream region and the upstream region in each case.

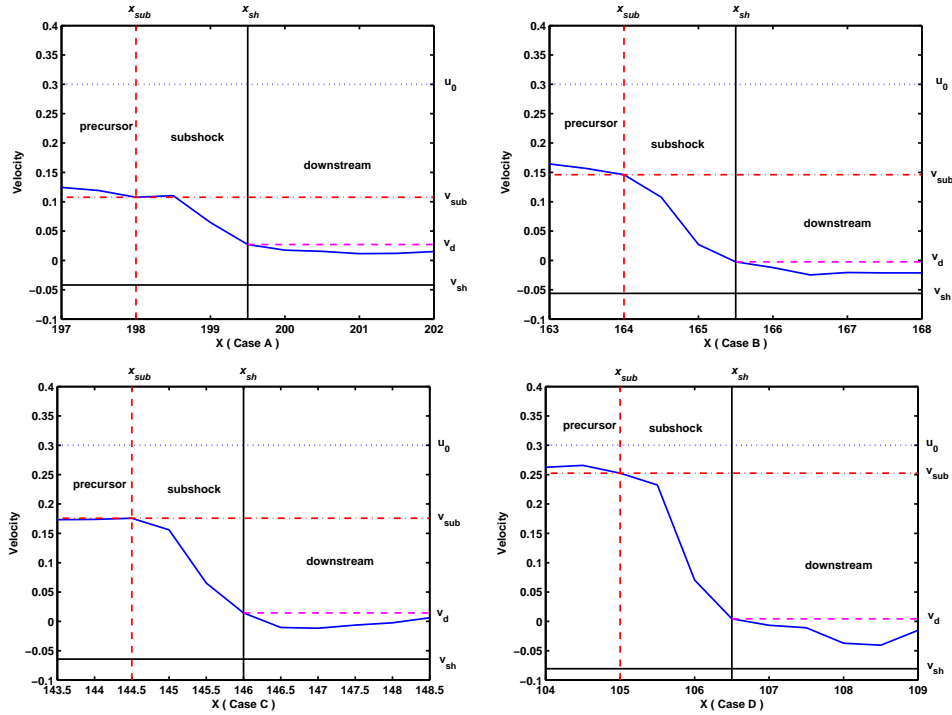


**Figure 3.** The subtle structures of the subshock in four cases at the end of simulation time. The drops of velocity in the subshock region are denoted by the values between  $V_{sub}$  and  $V_d$  in each case.

the thermal mean free path of the thermalized particles in the downstream region. So the subshock's velocity can be defined by the value of the  $V_{sub}$  in each case. The velocity  $V_d$  represents the downstream bulk speed at the shock position at the end of the simulation. The bottom solid line

denotes the backward shock evolutionary velocity  $V_{sh}$  with an increasing value from the Cases A, B, and C to D, respectively. Because the subshock is the fraction of the total shock, we can calculate the subshock's compression ratio  $r_{sub}$  according to the total shock compression ratio  $r_{tot}$  as

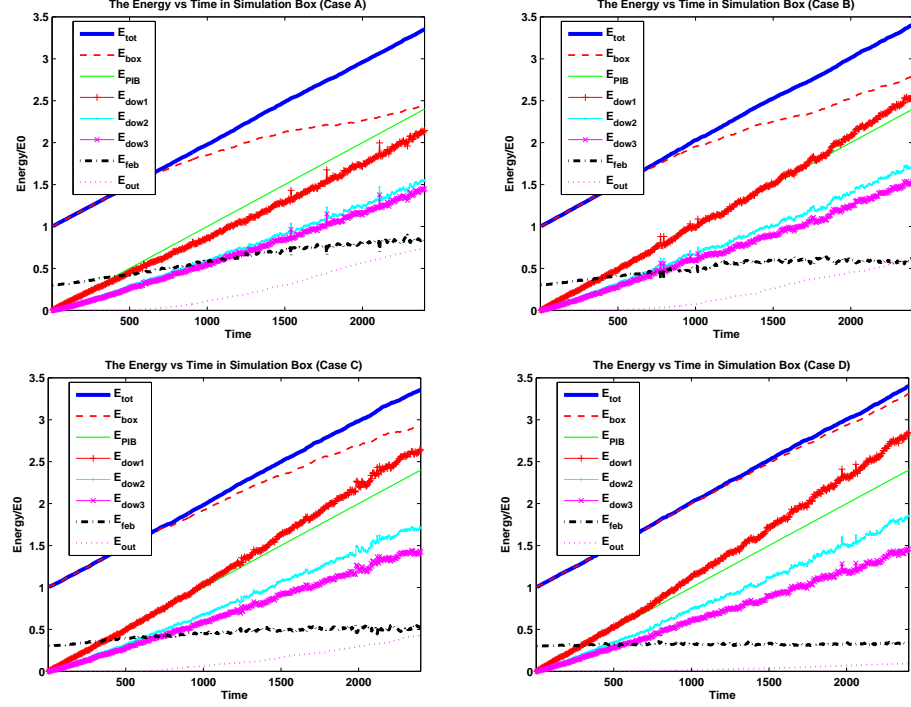


**Figure 4.** Various energy values vs. time (all normalized to the initial total energy  $E_0$  in the simulation box) in each case. All quantities are calculated in the box frame.

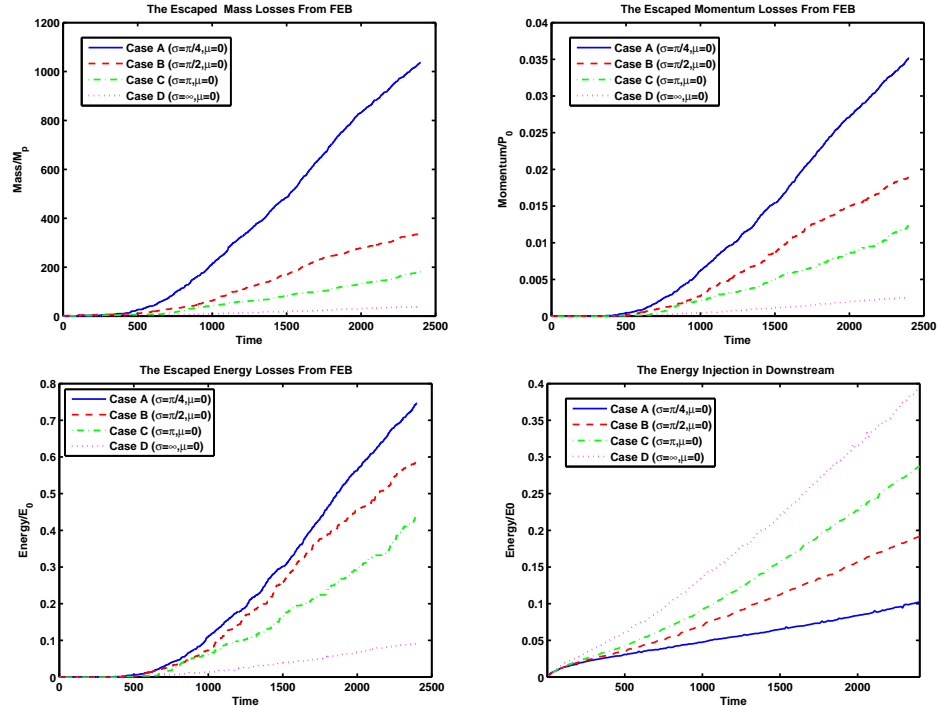


**Figure 5.** The four plots denote the mass losses, momentum losses, energy losses via the FEB and the injected energies in the downstream region, respectively. The solid line, dashed line, dash-dotted line and the dotted line represent the cases A, B, C and D in each plot, respectively. The units are normalized to the initial box proton mass  $M_p$ , initial box momentum  $P_0$  and initial box energy  $E_0$ , respectively.

following.

$$r_{sub} = \frac{V_{sub}}{U_0} \times r_{tot} \quad (4)$$

### 3.2. Energy injection & losses

We have monitored the energy of the total particles over the time in different regions with respect to all cases. Figure 4 shows all the types of energy functions with time. The  $E_{tot}$  is the energy summation of the total particles in the total simulation system over the time. The  $E_{box}$  is the energy summation of the actual particles in the simulation box over the time. The  $E_{pib}$  is the energy summation of the continuous new particles enter into the simulation box from the “preinflow box” over the time. The  $E_{dow1}$  is the energy summation of the all particles in the downstream region over the time. The  $E_{dow2}$  is the energy summation of the all particles which their local velocity over the value of the initial velocity  $U_0$  in the downstream region over the time. The  $E_{dow3}$  is the energy  $E_{dow2}$  minus the  $E_{inj}$ , which is the initial individual particle’s energy (i.e.  $\varepsilon_k = 1/2mU_0^2 + 1/2mv_k^2$ ) summation of the injected particles from the “thermal pool” at the local velocity of  $V_L = U_0$  to the superthermal particles in the downstream region, over the time. The  $E_{feb}$  is the energy summation of the total particles in the precursor region over the time. The  $E_{out}$  is the energy summation of the all particles escaped from the FEB over the time. Clearly, the total energy  $E_{tot}$  in the simulation system at any instant in time is not equal to the actual box energy  $E_{box}$  at any instant in time in each plot. It is evident from the real-time functions in Figure 4, the non-linear divergence between the curves for  $E_{box}$  and  $E_{tot}$  is produced with a decreasing value from the Cases A, B, and C to D, respectively. Also, the energy loss function  $E_{out}$  is produced with a decreasing value from the Cases A, B, and C to D, respectively. Simultaneously, the difference between the energy functions  $E_{dow2}$  and  $E_{dow3}$  shows an increasing energy injection  $E_{inj}$  from the Cases A, B, and C to D, respectively.

As shown in Table 3, all the listed results of the particle injection and losses in each case are calculated at the end of the simulation (i.e.  $T_{max}=2400$ ). The  $M_{loss}$ ,  $P_{loss}$  and  $E_{loss}$  are the mass loss, the momentum loss and the energy

loss of the particles escaped via to the FEB, respectively. The  $E_{feb}$ ,  $E_{inj}$ ,  $E_{tot}$ , and  $E_{dow1}$ , with the unit of an initial box energy  $E_0$ , are all the energy values in their respective statistical volumes at the end of simulation. The  $R_{inj}$  represents the rate of the energy injection  $E_{inj}$  with the total downstream energy  $E_{dow1}$  at the end of simulation. And the  $R_{loss}$  represents the rate of the energy losses  $E_{loss}$  with the total energy in the system  $E_{tot}$  at the end of the simulation. These correlations are presented as follows.

$$E_{inj} = E_{dow2} - E_{dow3} \quad (5)$$

$$R_{inj} = E_{inj}/E_{dow1} \quad (6)$$

$$E_{loss} = E_{out} \quad (7)$$

$$R_{loss} = E_{out}/E_{tot} \quad (8)$$

For the comparison, the mass loss, momentum loss, energy loss and energy injection functions with the time are calculated in Figure 5. Since the simulation system are based on the computational calculations, the existence of the energy losses is inevitable. Figure 5 show that the mass loss, momentum loss, and the energy loss functions with a decreasing value in any instant of time from the Cases A, B, and C to D, respectively. Among of these loss functions, the energy loss function shows a decreasing values of  $(E_{loss})_A = 0.7468$ ,  $(E_{loss})_B = 0.5861$ ,  $(E_{loss})_C = 0.4397$ , and  $(E_{loss})_D = 0.0904$  at the end of the simulation from the Cases A, B, and C to D, respectively. On the contrary, the energy injection function show an increasing values of  $(E_{inj})_A = 0.1025$ ,  $(E_{inj})_B = 0.1912$ ,  $(E_{inj})_C = 0.2873$ , and  $(E_{inj})_D = 0.3955$  at the end of the simulation from the Cases A, B, and C to D, respectively. By of the existence of the energy losses in the simulation system, the shock compression ratios are naturally affected according to the Rankine-Hugoniot conditions. Therefore, the difference of the energy losses or injection produced by the prescribed scattering angular distributions can directly affect all aspects of the simulated shock including the subtle shock structures, compression ratios, maximum energy particles, and the energy spectrums, as well as other aspects. It is just this self-consistent injection mechanism and PIC techniques which allow the energy injection and loss functions to be obtained. So the further energy analysis for the diffusive shock acceleration could be done easily.

### 3.3. Maximum energy

We select some individual particles from the downstream region at the end of the simulation for obtaining the plots in the coordinates of the phase, space and time. The trajectories of the selected particles are shown in Figure 6. Among of these selected particles in each case, one of these trajectories clearly shows the fully acceleration processes of the maximum energy particle which undergoes the multiple crossings with the shock front. The maximum value of the local velocity marked in each plot shows an increasing values of  $(VL_{max})_A = 11.4115$ ,  $(VL_{max})_B = 14.2978$ ,  $(VL_{max})_C = 17.2347$ , and  $(VL_{max})_D = 21.6285$  from the Cases A, B, and C to D, respectively. And the corresponding statistical error of the local velocity in each case is listed in the Table 3. Consequently, The cutoff energy at the “power-law” tail in the energy spectrum is given with an increasing value of  $(E_{max})_A=1.23$  MeV,  $(E_{max})_B=1.93$  MeV,  $(E_{max})_C=2.80$  MeV and  $(E_{max})_D=4.41$  MeV from the Cases A, B, and C to D, respectively. As for the escaped particles, owing to their energies are higher than the cutoff energy, they are not available in the system by of their escaping via the FEB eventually. Since the FEB is a constant distance (i.e.  $X_{feb} = 90$ ) in front of the shock and maintains

**Table 2.** The results of the shock simulation

Items	Case A	Case B	Case C	Case D
$X_{sh}$	199.5	165.5	146	106.5
$X_{FEB}$	109.5	75.5	56	16.5
$V_{sub}$	0.1075	0.1460	0.1757	0.2525
$V_d$	+0.0207	-0.0024	+0.0144	+0.0045
$V_{sh}$	-0.0419	-0.0560	-0.0642	-0.0806
$r_{tot}$	8.1642	6.3532	5.6753	4.7209
$r_{sub}$	2.9258	3.0910	3.3246	3.9734
$\Gamma_{tot}$	0.7094	0.7802	0.8208	0.9031
$\Gamma_{sub}$	1.2789	1.2174	1.1453	1.0045
$VL_{max}$	11.4115	14.2978	17.2347	21.6285
$ErrorBar$	+0.0017	-0.0022	+0.0014	-0.0025

**Table 3.** The results of the particle injection and losses

Items	Case A	Case B	Case C	Case D
$M_{loss}$	1037	338	182	38
$P_{loss}$	0.0352	0.0189	0.0123	0.0025
$E_{loss}$	0.7468	0.5861	0.4397	0.0904
$E_{tot}$	3.3534	3.4056	3.3574	3.4025
$E_{feb}$	0.8393	0.5881	0.5310	0.3397
$E_{dow1}$	2.1451	2.5612	2.6359	2.6903
$E_{inj}$	0.1025	0.1912	0.2873	0.3955
$R_{inj}$	4.78%	7.47%	10.90%	14.70%
$R_{loss}$	22.27%	17.21%	13.10%	2.66%

Notes: The units of mass, momentum, and energy are normalized to the proton mass  $M_p$ , initial total momentum  $P_0$  and initial box energy  $E_0$ , respectively.



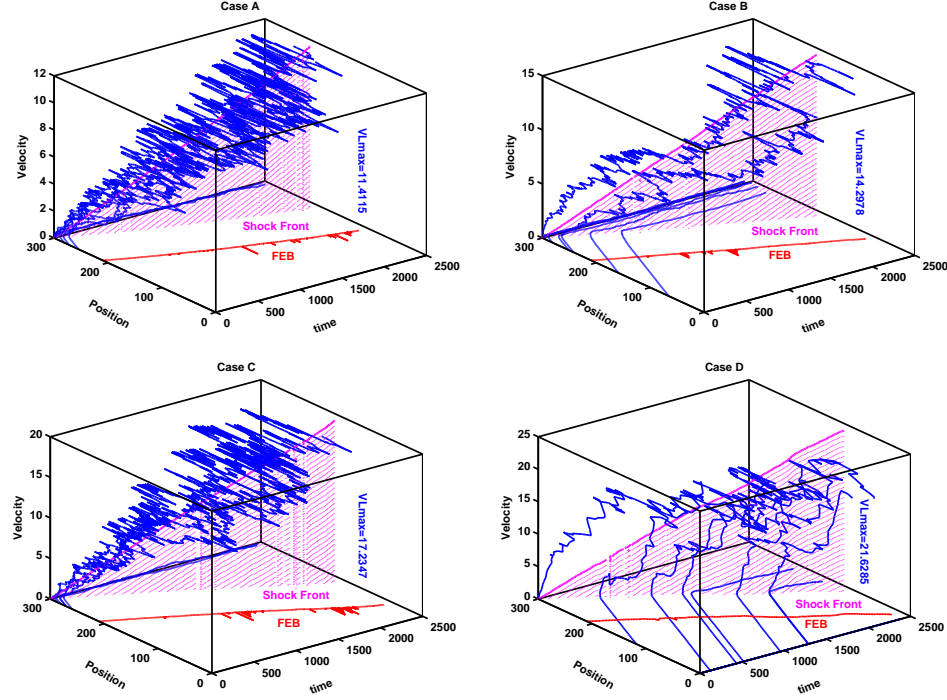


**Figure 6.** The individual particles with their local velocities vs their positions with respect to time in each plot. The shaded area indicates the shock front, the solid line in the bottom plane denotes the position of the FEB in each case, respectively. Some irregular curves trace the individual particle's trajectories near the shock front with time. The maximum energy of accelerated particles in each case is marked with the value of the local velocity, respectively.

the parallel moving of the shock front in each case, once an accelerated particle diffuse beyond the position of the FEB, this particle will be excluded from the system. The Table 3 shows the numbers of the escaped particles at the end of the simulation with a decreasing mass losses of  $(M_{loss})_A = 1037$ ,  $(M_{loss})_B = 338$ ,  $(M_{loss})_C = 182$ , and  $(M_{loss})_D = 38$  from the Cases A, B, and C to D, respectively. Also the energy statistical data exhibit the energy loss rate with a decreasing value of  $(R_{loss})_A = 22.27\%$ ,  $(R_{loss})_B = 17.21\%$ ,  $(R_{loss})_C = 13.10\%$ , and  $(R_{loss})_D = 2.66\%$  from the Cases A, B, and C to D, at the end of the simulation, respectively.

Except for the maximum energy particles, there are also common energetic particles are shown in the plots with some of them obtained finite energy accelerations from the multiple crossings with the shock and some of them do not have additional energy gains owing to their lack of probability for crossing back into the precursor. If the cutoff energy of the simulation system is not effected by the prescribed scattering angular distribution, these maximum energy particles in different cases should be identical or at least be similar equal in the range of error bar. But the actual difference of the cutoff energy particles in different cases should be contributed by the different prescribed scattering angular distributions dominating the different energy injection.

### 3.4. Heating, acceleration & spectrum

As shown in Figure 7, the four energy spectrums with the “power-law” tails represent the four cases, averaged over the precursor region, at the end of simulation, respectively. The thin solid curve with a narrow peak is the initial Maxwellian distribution in the shock frame. The four extended energy spectrums are all consist of two very different parts: the low energy part and the high energy part. The low energy part in the left side of the initial spectrum, range from the low energy to the central peak, shows the “irregular fluctuation” in each case. The high energy part in the right side of the

initial spectrum, range from the central peak energy to the cutoff energy, shows the smooth “power-law” tail in each case. The “irregular fluctuation” indicates that the supersonic upstream fluid slows down in precursor region and its translational energy begin to convert into the irregular random energy. The “power-law” tail implies that the injected particles from the “thermal pool” in the downstream region scatter into the precursor region crossing the shock front for multiple energy gains and become into the superthermal particles.

Look at extended curves closely, the low energy part in each case has a clearly joint point with the high energy part. And the joint point show an increasing energy value from the Cases A, B, and C to D, respectively. Consequently, the corresponding cutoff energy at the “power-law” tail in the precursor region also shows an increasing value from the Cases A, B, and C to D, respectively. This joint point should be correlated to the average thermal velocity in the downstream region. As shown in the Figure 8, the four thermal velocity functions are averaged over the downstream region with the time. And each curve denotes the evolution of the average thermal velocity with the time and shows a constant after a certain duration (i.e.,  $t = 500$ ). Eventually, the average thermal velocity  $V_{th}$  shows an increasing value from the Cases A, B, and C to D, at any instant of time, respectively. As expected, the energy injection from the “thermal pool” in the downstream region shows an increasing value from the Cases A, B, and C to D, respectively. Therefore, as show in the Figure 7, the energy spectrum in the precursor region shows an increasing hard spectral slope as the dispersion value  $\sigma$  of the Gaussian scattering angular distribution increases. This correlation of the energy spectrum averaged over the precursor region with the prescribed scattering law is consistent with the energy spectrum averaged over the downstream region.

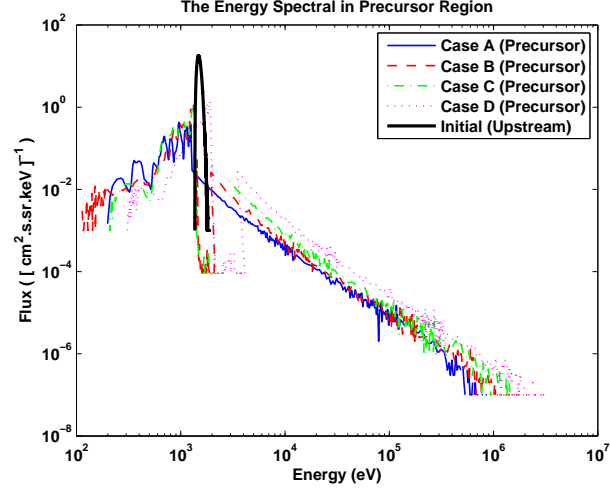


**Figure 7.** This plot represents the energy spectrums on the precursor region at the end of the simulation. The thick solid line with a narrow peak at  $E = 1.3105 \text{ keV}$  represents the initial Maxwell energy distributions. The solid, dashed, dash-dotted and dotted extended curves with the “power-law” tail present the energy spectrum corresponding to Cases A, B, C and D, respectively. All these energy spectrum are calculated in the same shock frame.

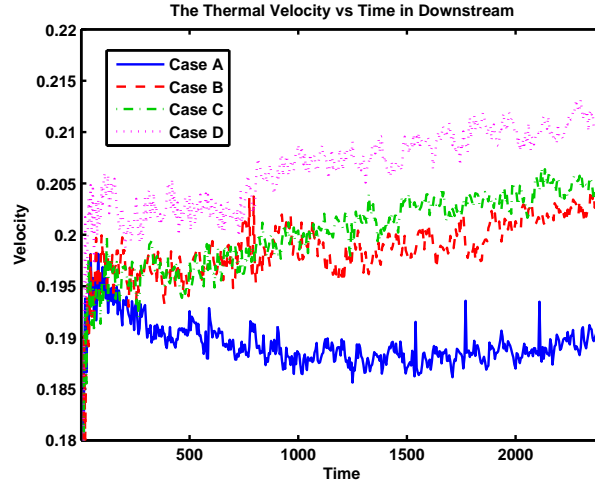


**Figure 8.** This plot denotes the average thermal velocity with the time in the downstream region in each case.



Generally, we could predict the power-law energy spectral index from diffusive shock acceleration theory:

$$dJ/dE \propto E^{-\Gamma} \quad (9)$$

where  $dJ/dE$  is the energy flux and the  $\Gamma$  is the energy spectral index. And the spectrum index can be calculated as following:

$$\Gamma_{tot} = (r_{tot} + 2)/[2 \times (r_{tot} - 1)]. \quad (10)$$

$$\Gamma_{sub} = (r_{sub} + 2)/[2 \times (r_{sub} - 1)]. \quad (11)$$

According to Equation 10 and Equation 11, we substitute the corresponding values of the compression ratio  $r$  in each case. Then, the two types of energy spectral indices  $\Gamma_{tot}$  and  $\Gamma_{sub}$  in each case are calculated. As listed in the Table 2, the total shock energy spectral index shows an increasing value of the  $(\Gamma_{tot})A=0.7094$ ,  $(\Gamma_{tot})B=0.7802$ ,  $(\Gamma_{tot})C=0.8208$ , and  $(\Gamma_{tot})D=0.9031$  from the Cases A, B, and C to D, respectively. However, the subshock's energy spectral index is a decreasing value of the  $(\Gamma_{sub})A=1.2789$ ,  $(\Gamma_{sub})B=1.2174$ ,  $(\Gamma_{sub})C=1.1453$ , and  $(\Gamma_{sub})D=1.0045$  from the Cases A, B, and C to D, respectively.

As shown in Figure 9, all of the values of the subshock's energy spectral index are more than one (i.e.  $\Gamma_{sub} > 1$ ), and the solid line denotes the subshock's energy spectral index with a decreasing value from the Cases A, B, and C to D as the energy injection increases, respectively. However, all of the values of the total shock's energy spectral index are less than one (i.e.  $\Gamma_{tot} < 1$ ), and the dashed line denotes the total shock's energy spectral index with an increasing value from the Cases A, B, and C to D as the energy injection increases, respectively. Simultaneously, as shown in Figure 10, the solid line denotes the subshock energy spectral index with a decreasing value from the Cases A, B, and C to D as the energy loss decreases, respectively. However, the dashed line denotes the total shock's energy spectral index with an increasing value from the Cases A, B, and C to D as the energy loss decreases, respectively. According to the diffusive shock acceleration theory, if the energy loss is limited to be the minimum, the simulation models based on the computer will more closely fit the realistic physical situation. The Figure 9 and Figure 10 indicate that the correlations of the energy spectral index with the energy injection or the energy losses are consistent with the energy spectral index is dependent on the prescribed multiple scattering angular distributions. As seen from the Cases A, B, and C to D, the subshock's energy spectral index and the total shock's energy spectral index are both approximating to the realistic value one (i.e.  $\Gamma \sim 1$ ) as the energy injection increases or as the energy loss decreases. As predicted, the Rankine-Hugoniot (RH) jump conditions allow to derive the relation of the compression ratio with the Mach number as:  $r = (\gamma_a + 1)/(\gamma_a - 1 + 2/M^2)$ .

For a nonrelativistic shock, the adiabatic index  $\gamma_a = 5/3$ , if the Mach number  $M \gg 1$ , then the maximum compression ratio should be 4. According the Rankie-Hugoniot conditions, the total shock compression ratio should be less than standard value 4, and the corresponding total shock's energy spectral index should be less than the standard value one for a nonrelativistic shock [Pelletier, 2001]. Simultaneously, we can see that if the energy injection achieves to the enough high level or the energy loss is limited to the enough low level, the subshock's energy spectral index will closely approximate the standard value of one. We present explicitly these relationships between the energy spectral indices, the energy injection or energy losses, and the prescribed scattering law. And these relationships will be very helpful to improve simulation models by the best choice of the prescribed scattering law. Using the prescribed scattering law instead of the assumption of the transparent function in the thermal leakage mechanism, as far as the injection problem is concerned, the dynamical Monte Carlo model based on the PIC techniques is nothing less than a fully self-consistent and time-dependent model.

#### 4. Summary and conclusions

In summary, we performed the dynamical Monte Carlo simulations using the Gaussian scattering angular distributions based on the Matlab platform by monitoring the particle's mass, momentum and energy at any instant in time. The specific energy injection and loss functions with time are presented. We successfully examine the correlation between the energy spectral index and the prescribed Gaussian scattering angular distributions by the energy injection and loss functions in four cases. Simultaneously, this correlation is further enhanced by using the radial reflective boundary (RRB).

In conclusion, the relationship between the energy injection or energy losses and the prescribed scattering law verify that the shock energy spectral index is surely dependent on the prescribed scattering law. As expected, the maximum energy of accelerated particles is correlated with the particle injection rate from the "thermal pool" to superthermal population. So we find that the energy injection rate increases as the standard deviation value of the scattering angular distribution increases. In these multiple scattering angular distribution scenario, the prescribed scattering law dominates the energy injection or the energy losses. So this self-consistent energy injection mechanism is capable to instead of the assumption of the thermal leakage injected function. Consequently, the cases applying anisotropic scattering angular distribution will produce a small energy injection and large energy losses leading to a soft energy spectrum, the case applying isotropic scattering angular distribution will produce a large energy injection and small energy losses leading to a hard energy

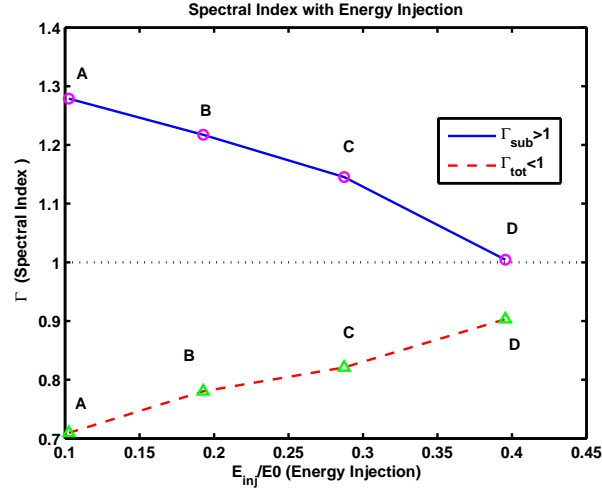


**Figure 9.** The plot shows the correlation of the energy spectral index vs the energy injection. The triangles represent the total energy spectral index of the all cases. The circles indicate the subshock's energy spectral index of all cases.

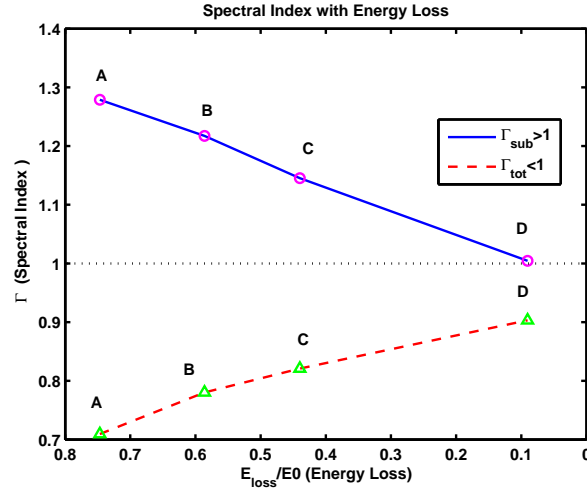


**Figure 10.** The plot shows the correlation of the energy spectral index vs the energy losses. The triangles represent the total energy spectral index of the all cases. The circles indicate the subshock's energy spectral index of all cases.

spectrum. These relationships will drive us to find a newly plausible prescribed scattering law which making the simulation model more close to the realistic physics.

**Acknowledgments.** The authors would like to thank Profs. Hongbo Hu, Siming Liu, Xueshang Feng, and Gang Qin for many useful and interesting discussions concerning this work. In addition, we also appreciate Profs. Qijun Fu and Shujuan Wang, as well as other members of the solar radio group at NAOC. This work was funded in part by CAS-NSFC grant 10778605 and NSFC grant 10921303 and the National Basic Research Program of the MOST (Grant No. 2011CB811401).

## References

- Axford, W.I., Leer, E., & Skadron, G., 1977 in *Proc. 15th Int. Cosmic Ray Conf. (Plovdiv)*, 132
- Bell, A. R., 1978, *Mon. Not. R. Astron. Soc.*, 182, 147.
- Bell, A. R., 2004, *Mon. Not. R. Astron. Soc.*, 353, 550.
- Blandford, R. D., & Ostriker, J. P. 1978, *Astrophys. J.*, 221, L29.
- Blasi, P., Amato, E., & Caprioli, D., 2007, *Mon. Not. R. Astron. Soc.*, 375, 1471
- Blasi, P., Gabici, S., & Vannoni, G., 2005, *Mon. Not. R. Astron. Soc.*, 361, 907
- Cane, H. V., von Rosenvinge, T. T., & McGuire, R. E., 1990, *J. Geophys. Res.*, 95, 6575.
- Caprioli, D., Kang, H., Vladimirov, A. E. & Jones, T. W., 2010, *Mon. Not. R. Astron. Soc.*, 407, 1773
- Ellison, D. C., Baring, M. G., & Jones, F. C. , 1996, *Astrophys. J.*, 473, 1029
- Ellison, D. C., Möbius, E. & Paschmann, G., 1990 *Astrophys. J.*, 352, 376
- Ellison, D. C., Blasi & Gabici , 2005, in *Proc. 29th Int. Cosmic Ray Conf. (India)*.
- Forslund, D. W. , 1990 *Space Sci. Rev.* 42, 3
- Giacalone, J. , 2004, *Astron. Astrophys.*, 609, 452.
- Gosling, J.T., Asbridge, J.R., Bame, S.J., Feldman, W.C., Zwicky, R. D., Paschmann, G., Sckopke, N., & Hynds, R. J. 1981, *J. Geophys. Res.*, 866, 547
- Hillas, 1984, *ARA&A*, 22, 425.
- Jones, F. C., & Ellison, D. C., 1991, *Space Sci. Rev.*, 58, 259.
- Kang H. & Jones T.W. 2007, *A. Ph.*, 28, 232

- Knerr, J. M., Jokipii, J. R. & Ellison, D. C. 1996, *Astrophys. J.*, 458, 641
- Krymsky, G. F., 1977, Akad. Nauk SSSR Dokl., 243, 1306
- Lagage, P. O., & Cesarsky, C. J., 1983, *Astron. Astrophys.*, 118, 223
- Lee, M. A., & Ryan, J. M., 1986, *Astrophys. J.*, 303, 829
- Lee, M. A., 2005, *Astrophys. J. (Supp.)*, 158, 38
- Leroy, M. M., Winske, D., Goodrich, C. C., Wu, C. S., & Papadopoulos, K., 1982, *J. Geophys. Res.*, 87, 5081
- Li, G., Zank, G. P., & Rice, W. K. M., 2003, *J. Geophys. Res.*, 108, 1082
- Li, G., Zank, G. P., & Verkhoglyadova, O. P., et.al. 2009, *Astrophys. J.*, 702, 998
- Malkov, M. A., Diamond, P. H., & Völk, H. J., 2000, *Astrophys. J.*, 533, 171
- Mitchell, D. G., Roelof, E. C., Sanderson, T. R., Reinhard, R., & Wenzel, K. P., 1983, *J. Geophys. Res.*, 88, 5635
- Niemiec, J., Pohl, M., Stroman, T., & Nishikawa, K.-I., 2008, *Astrophys. J.*, 684, 1174.
- Ostrowski, M., 1988, *Mon. Not. R. Astron. Soc.*, 233, 257
- Pelletier, G. 2001, *Lecture Notes in Physics*, 576, 58
- Pelletier, G., Lemoine, M. & Marcowith, A., 2006, *Astron. Astrophys.*, 453, 181.
- Spitkovsky, A., 2008, *Astrophys. J.*, 673, L39.
- Vainio, R., & Laitinen, T., 2007, *Astrophys. J.*, 658, 622.
- Vladimirov, A., Ellison, D. C., & Bykov, A., 2006, *Astrophys. J.*, 652, 1246
- Wang, X., & Yan, Y., 2011, *Astron. Astrophys.*, 530, A92.
- Winske, D., & Omid, N., 1996, *J. Geophys. Res.*, 101, 17287–17304.
- Zank, G., Rice, W.K.M., & Wu, C. C., 2000, *J. Geophys. Res.*, 105, 25079
- Zirakashvili, V. N. & Aharonian, F. A., 2010, *Astrophys. J.*, 708, 965

---

Xin, Wang, (wangxin@nao.cas.cn)

Yihua, Yan, (yyh@nao.cas.cn)